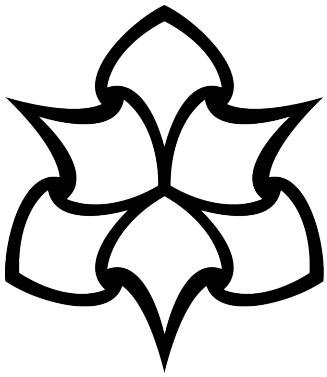

ACS Catalysis

pubs.acs.org/acscatalysis Research Article

Supported Oxygen Evolution Catalysts by Design: Toward Lower Precious Metal Loading and Improved Conductivity in Proton Exchange Membrane Water Electrolyzers

Yagya N. Regmi, Eden Tzanetopoulos, Guosong Zeng, Xiong Peng, Douglas I. Kushner, Tobias A. Kistler, Laurie A. King, and Nemanja Danilovic*

Cite This: https://dx.doi.org/10.1021/acscatal.0c03098 Read Online

ACCESS | Metrics & More | Article Recommendations | Supporting Information

ABSTRACT: Reducing the precious metal content of water oxidation catalysts for proton-exchange-membrane water electrolyzers remains a critical barrier to their large-scale deployment. Herein, we present an engineered architecture for supported iridium catalysts, which enables decreased precious metal content and improved activity and conductivity. The improvement in performance at lower precious metal loading is realized by the deposition of a conformal layer of platinum nanoparticles on titanium dioxide (TiO_2) using a facile photoreduction method to prepare conductive layer coated supports (CCSs). Platinum nanoparticles are homogeneously dispersed on TiO_2, and the conductivity of the subsequent catalysts with 39 wt % precious group metal loadings is significantly higher than the commercial 75 wt % loaded IrO_2-TiO_2 catalysts. The conformal conductive layer also maintains an enhanced conductivity and electrochemical activity upon thermal annealing when compared to catalysts without the conductive layer and nonconformal heterogeneous conductive layer. The iridium mass activity from half-cell studies shows a 141% improvement for CCS supported catalysts at 42% lower loadings compared to the commercial catalysts. The conductive layer also improves the single cell electrolyzer performance at a similar catalyst loading in comparison to a commercial state-of-the-art catalyst. We correlate the physical properties of the engineered catalysts with their electrochemical performance in electrolyzers to understand structure−activity relationships, and we anticipate further performance improvements upon synthesis and materials optimizations.

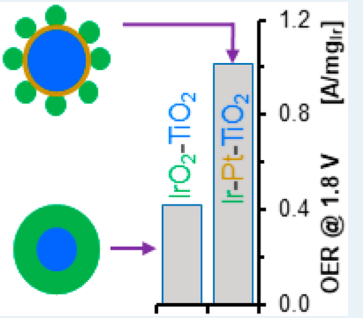

KEYWORDS: *proton exchange membrane electrolyzers, water splitting, oxygen evolution reaction, supported electrocatalysts, iridium catalysts, photoreduction, membrane electrode assembly*

INTRODUCTION

Electrochemical hydrogen generation has the potential to decarbonize the energy sector, enabling high renewable energy penetration through long-term energy storage and conversion.[1,2] Additionally, deep decarbonization of industrial processes such as food production (ammonia synthesis), oil refining, and steel manufacturing can be realized if the "green" hydrogen from water splitting replaces hydrogen generated via routes that release carbon dioxide and other harmful byproducts.[3,4] Annually, more than 95% of the 70 million tons of hydrogen is produced globally from hydrocarbons via steam methane reforming (SMR), water−gas shift, and coal gasification, among other processes.[5] Electrolysis currently accounts for only 4% of hydrogen production. Proton-exchange-membrane (PEM)-based water splitting is one promising technology to displace SMR, however several cost-cutting measures are necessary to achieve the goal. One such measure is either to use curtailed renewable electricity or to reach power purchase agreements to reduce the feedstock cost (electricity). Eventual widespread deployment of PEM water electrolyzers (PEMWEs) is projected to render the electrochemical stack as the dominant cost, and the catalyst layers (CLs) as the most expensive components in the stack.[6] Today, the CLs account for about 5% of the total cost of the stack, but this value is projected to increase as electrochemical hydrogen production is scaled up from kW to GW.[7] Thus, by simultaneously lowering the feedstock costs and either replacing or lowering the platinum group metal (PGM) loadings in catalyst layers (CLs), it will be possible to lower the price of green H_2 to the SMR range.[5] The techno-economic barrier emanating from high PGM loadings needs to be surmounted to enable large-scale (TW) electrochemically generated hydrogen to become economically competitive with hydrogen generation from SMR.[7] The balance of plant and balance of cell costs are anticipated to decrease with high-

Received: July 16, 2020
Revised: September 28, 2020

https://dx.doi.org/10.1021/acscatal.0c03098
ACS Catal. XXXX, XXX, XXX−XXX

throughput manufacturing. Conversely, PGM costs are expected to remain high due to their limited abundance in the earth's crust, of which Ir is far rarer than Pt.[8] To reduce the precious metal loading in PEM electrolyzers, various strategies including the use of non-PGM catalysts and engineering CLs with lower loadings of PGM catalysts supported on low-cost substrates have been explored.[9−13] For example, King et al. recently reported the use of CoP as the cathode catalyst on PEMWE,[14] and Alia et al. have shown the promising stability of various low Ir-loaded anode CLs.[15] While a diverse library of non-PGM materials for cathodic hydrogen evolution reaction (HER) in PEMWE has been developed,[16] analogous materials for anodic oxygen evolution reaction (OER) for PEMWE are yet to be identified.[17,18] While the ultimate goal is to mitigate the usage of PGM catalysts, the need for short and midterm strategies to lower the PGM loading represents a critical development. To this end, one of the most promising strategies is to develop stable and conductive electrocatalyst supports akin to the carbon supports currently deployed in the CLs of PEM fuel cells.

Supports employed in PEMWE anodes must withstand the highly corrosive acidic (pH < 1) and oxidizing (>2 V) conditions.[19] Furthermore, the support needs to be conductive. Under these conditions, most metals will readily oxidize and form insulating layers, while the few that can withstand the harsh conditions are just as expensive as Ir. While some metal oxides can withstand the corrosive conditions, most are poor conductors.[20,21] Strategies to boost conductivity of metal oxides such as doping titanium oxide (TiO_2) and niobium oxide have shown improved conductivity over undoped oxides; however, their conductivity is lower than that of metals and the dopants are also known to leach out over time, thereby further reducing conductivity and stability.[22,23]

As depicted in Figure 1a, for unsupported iridium, the bulk of the catalyst particle functions as the conductive support with only the surface Ir atoms participating in catalysis. Currently, PEMWE anodes typically utilize unsupported Ir resulting in relatively large PGM catalyst particles and clusters on the order of 80 nm and larger that are applied at high loading (>1 mg_{Ir}/cm^2) to maintain adequate CL thickness, connectivity, and porosity.[24,25] A strategy to reduce PGM loading on PEMWE anodes has been the use of non-PGM cores such as TiO_2 with a shell of Ir catalysts (Ir-TiO_2) as illustrated in Figure 1b. However, in order to maintain conductivity of the shell, Ir loadings in excess of 50 wt % Ir are necessary,[26] as demonstrated for half-cell OER and electrolyzer performances.[2,11,19,27,28]

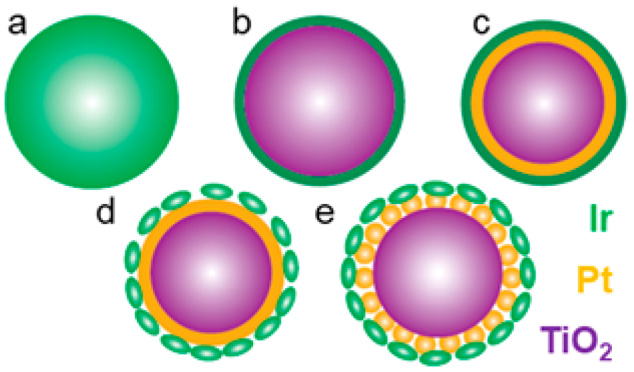

Figure 1. Schematics of: (a) bulk Ir catalyst, (b) traditional >50 wt % Ir shell coated on TiO_2 core, (c) proposed catalyst with Pt or Au intermediate layer between Ir and TiO_2, (d) nanostructuring strategy to reduce Ir loading without losing overall catalyst surface area, and (e) nanostructuring of both the catalyst and conductive intermediate layer to lower PGM loading without losing the catalyst surface area or conductivity.

We propose modifying the core−shell architecture by adding a very thin layer of conductive and electrochemically stable interfacial material, namely Pt or Au, between the TiO_2 core and the Ir catalyst (Figure 1c−e). Such conductive layers can also provide the possibility to further nanostructure the Ir catalyst and the conductive layer itself to reduce overall PGM loading without compromising specific activity, as depicted in Figure 1d,e. This strategy represents a new pathway to reduce Ir loading without compromising the activity and conductivity. Replacing Ir with Pt or Au has economic advantages as well in the short and medium terms, that is, until earth-abundant elements replace PGMs as OER catalysts. Pt and Au are a magnitude more abundant than Ir on the earth's crust.[29]

Our inspiration comes from the use of Pt as a corrosion-resistant protective coating in PEMWE anode porous transport layers and bipolar plates, where they are known to withstand over 50,000 h of service.[30−33] These precious metal-coated TiO_2 conductive catalyst supports (CCSs) also offer a pathway to enhance mass transport in the CLs by changing the TiO_2 particle size and thus improving the CL porosity. Akin to the roles carbon supports play in Pt/C CLs,[34] we advocate that the use of a substrate has the potential to increase the CL thickness, improve the distribution of Ir at low loadings, and renders an extra degree of flexibility in design by allowing for different Ir wt % on the support to be used. Generation of targeted materials interfaces at the nanoscale presents additional opportunities to engineer highly efficient and stable active sites.[35]

In this paper, we synthesized CCS particles with thin layers of either Pt or Au nanoparticles prepared by a photochemical (PC) reduction deposition method (Table S1). As a control, CCSs were also synthesized using an incipient wetness impregnation (WI) method. In both systems, Ir was subsequently deposited on the CCSs using the WI method. Conductivities were measured using an in-house assembled DC conductivity setup,[36] and catalyst activities toward the oxygen evolution reaction (OER) were evaluated in a rotating disk electrode (RDE) and in a PEMWE. Throughout, we compare the performance with state-of-the-art commercial catalysts and previous investigations using supported Ir catalysts from the literature. We also correlate the activities with the physical characteristics of the catalysts using scanning and transmission electron microscopy (SEM and TEM), energy dispersive X-ray spectroscopy (EDS), X-ray photoelectron spectroscopy (XPS), and X-ray diffraction (XRD). Our findings provide rational pathways toward engineering more efficient and stable active sites at the support, conductive layer, and catalyst surfaces and interfaces.

EXPERIMENTAL SECTION

Photochemical Synthesis of CCS. A TiO_2 nanoparticles (<100 nm, 42−52 wt % in xylene, Sigma-Aldrich) slurry (5 mL) is added to 15 mL of deionized water (15 mL) in a centrifuge vial and vortexed. The suspension is centrifuged at 3500 rpm (700g) for 10 min before the supernatant is decanted and the precipitate is resuspended in deionized water

https://dx.doi.org/10.1021/acscatal.0c03098
ACS Catal. XXXX, XXX, XXX−XXX

(20 mL). The centrifugation and washing are repeated 4 times. The final TiO_2 precipitate is dried under vacuum at 60 °C for 12 h. Dried TiO_2 nanoparticles (200 mg) are added to deionized water (50 mL) and combined with an appropriate mass of chloroplatinic or chloroauric acid (Fischer Scientific) to achieve 25 wt % metal on TiO_2. The combined materials are stirred for 20 min to prepare a homogeneous mixture. The mixture is placed under a solar simulator equipped with a Xe lamp and AM1.5G filter, while stirring for 4 h to allow the deposition of gold or platinum nanoparticles onto the TiO_2 nanoparticle substrates (Supporting Video S1).[37] The solution is then centrifuged three times at 9000 rpm (7000*g*) for 15 min each. After each cycle, the supernatant is disposed of, and the 50 mL centrifuge vial was filled completely with deionized water and sonicated for 5 min before returning to the centrifuge.

Incipient Wetness Impregnation and Thermal Reduction Synthesis. An appropriate mass of dried TiO_2 nanoparticles is placed in a mortar and pestle. The exact mass of chlorometallic salts of Pt and Au is dissolved in acetone (2 mL, VWR Chemicals). Then, the chlorometallic salts are added dropwise to the TiO_2 powder while continuously grinding with the pestle. The resulting mixture is transferred to a quartz boat and placed in a tube furnace. The temperature is ramped to 400 °C at 10 °C/min under a reducing atmosphere (5% H_2 in Ar). After dwelling at 400 °C for 2 h, the temperature is allowed to naturally cool down to room temperature. On both the Au- and Pt-coated CCSs, 25 wt % Ir is deposited using the incipient wetness impregnation method as well as to prepare Ir-Pt/Au-TiO_2-PC/WI catalysts. Therefore, PC and WI indicate the synthesis pathway for the deposition of the Pt and Au conductive layer onto TiO_2, with Ir always deposited using WI on CCS.

Thermal Oxidation of CCS Supported Ir Catalysts. The catalysts are loaded on quartz boats and placed inside a furnace. The temperature is ramped at 10 °C/min to 400 °C under ambient conditions. The furnace temperature is kept at 400 °C for 2 h and then naturally allowed to cool down to room temperature.

Physical Measurements. XRD plots are recorded in Bragg−Brentano optics geometry with a Cu Kα source on a Rigaku SmartLab instrument. SEM micrographs are obtained using a SEM FEI Quanta 250 FEG equipped with a Bruker Quantax 200 EDX detector. XRF measurements are carried out using a Bruker M4 Tornado Micro-XRF. STEM micrographs were acquired using a 200 kV FEI monochromated F20 UT Tecnai instrument. The TEM-EDX maps are collected on a FEI TitanX 60−300 microscope equipped with a Bruker windowless EDS detector with a solid angle of 0.7 steradians. XPS data are collected on a Kratos Axis Ultra DLD system at a takeoff angle of 0° relative to the surface normal at room temperature. A monochromatic Al Kα source ($h\nu$ = 1486.6 eV) is used to excite the core level electrons of the material. Pt 4f, Ir 4f, Ti 2p, C 1s, and O 1s core levels are collected, with a pass energy of 20 eV, step size of 0.05 eV, and 8 sweeps each to obtain a good signal-to-noise ratio. The survey spectra (Figure S1) are acquired with a pass energy of 160 eV, step size of 1 eV, and 3 sweeps. The measurements are performed at ultrahigh-vacuum conditions (7.5×10^{-9} Torr).

Conductivity Measurements. A homemade DC conductivity setup was used to measure the particle conductivity.[36] Briefly, the catalyst powder was sandwiched between copper electrodes and compressed to 200 lb/in^2, the thickness was measured, and an $I-V$ curve was generated from −50 to 50 mV using a potentiostat (SP300, BioLogic). The catalyst conductivity was extracted from the slope of the curve and the catalyst thickness.

Electrode Preparation. The electrochemical measurement system and methods are adapted from earlier reports.[38] The gold disk working electrode is prepared by polishing with a 0.05 μm alumina slurry. The disk is rinsed and bath sonicated for 30 s to remove residual slurry and impurities. The disk is rinsed again and dried via a compressed nitrogen air gun. The glassware is cleaned by rinsing in ultrapure water (18.2 MΩ, Milli-Q), boiling for 1 h, and rinsing again. Catalyst inks are coated as a thin film layer on a polished gold tip working electrode (5 mm diameter). To prepare the inks, catalyst powder (3.5 mg) is combined with water (7.6 mL), 2-propanol (2.4 mL, VWR), and Nafion solution (40 μL, 5 wt % in alcohol, Ion Power). The catalyst suspension was bath sonicated for 20 min. Ten μL of the well-dispersed catalyst ink was pipetted onto the gold disk surface of the working electrode as it rotated on an inverted RDE at 100 rpm to distribute the ink evenly. The RDE speed is increased to 700 rpm and allowed to dry for 15−20 min until it was completely dry.

Electrochemical Measurements (RDE). Electrochemical measurements are performed using a Pine Instrument RDE and SP-300 potentiostat from BioLogic Science Instruments. The activities are recorded in 0.1 M $HClO_4$ electrolyte at 25 °C. A gold wire and dynamic hydrogen electrode (DHE) are used as the counter and reference electrodes, respectively. All potentials are adjusted to RHE. Once set up, the system is purged with ultrahigh-purity Ar for 15 min before the working electrode is placed in the electrolyte, and the electrochemical measurements are recorded. Commercial supported baseline catalyst, Elyst Ir75 0480, IrO_2-TiO_2 (75 wt % Ir) on TiO_2, is purchased from Umicore.

The 50 preliminary cyclic voltammetry (CV) scans are recorded at a 500 mV/s between 0.025 and 1.5 V. An additional 3 CV scans are run at a rate of 20 mV/s between 0.025 and 1.0 V. The 50 conditioning CV cycles are then collected from 1.2 to 1.8 V at 100 mV/s and 2500 rpm. Five OER activity CVs are then recorded at 20 mV/s. The short-term stability of selected samples is evaluated at 1.8 V and 2500 rpm.

Membrane Electrode Assembly. The fabrication of the membrane electrode assembly (MEA), the cell integration and testing have been described elsewhere.[39] In brief, cathode half-cell catalyst-coated membranes using Nafion N117 (Ion Power) were prepared as described earlier on a Sono-Tek Exactcoat spray coater to achieve 0.3 mg/cm^2 Pt loading (45.6 wt % Pt/C, Tanaka). Carbon gas-diffusion layers with a microporous layer (29 BC, Sigracet) were used on the cathode. The spray coating is not suitable for TiO_2 supported anode catalysts, since the supported catalyst particles precipitate readily on the syringe, delivery tubes, and nozzle head.[11] Thus, a modified slot-die method was utilized.[40] In brief, 1 mL of water, catalyst, and Nafion (11.6 wt % of the catalyst) were added in a centrifuge tube and sonicated using a probe sonicator. The ink was then immediately cast on the N117 membrane secured in place over the vacuum hot plate of the Sono-Tek Exactcoat at 50 °C. The catalyst loading was determined using an in-house prepared calibration curve based on XRF intensity counts. Titanium porous transport layers (Proton OnSite/NEL) were used on the anode after wet

https://dx.doi.org/10.1021/acscatal.0c03098
ACS Catal. XXXX, XXX, XXX−XXX

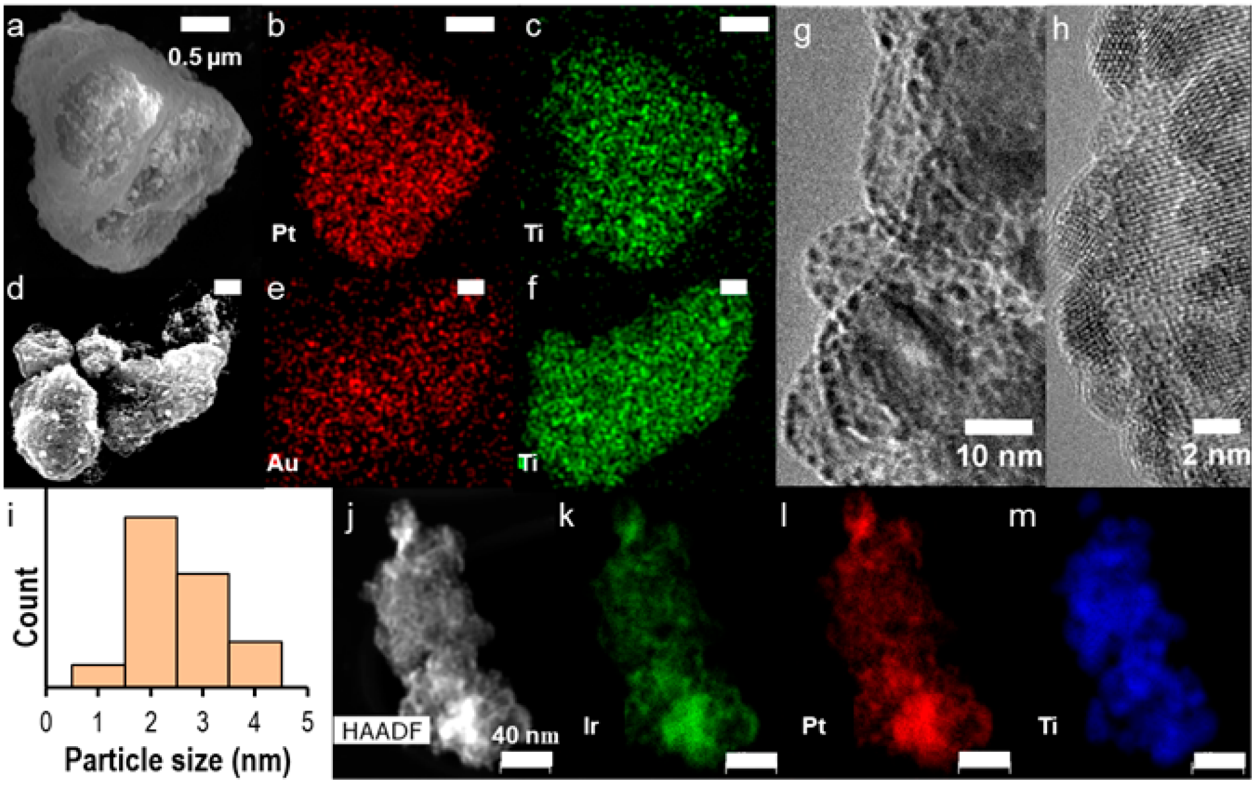

Figure 2. SEM image (a) and corresponding EDS maps (b and c) of Pt-TiO_2-PC. SEM image (d) and EDS maps (e and f) of Au-TiO_2-PC. TEM image (g), high-resolution TEM (h) and Pt particle size distribution of 100 Pt nanoparticles (i) of Pt-TiO_2-PC. High-angle annular dark-field (HAADF) image (j) and EDS maps (k–m) of Ir-Pt-TiO_2-PC-ann. All scale bars in (a–f) are 0.5 μm and scale bars in (j–m) are 40 nm. EDS spectra corresponding to EDS maps above are in Figures S5 and S6.

proofing with 3.5% PTFE (DISP 30, Ion Power). Ten mil and 7 mil PTFE sheets (McMaster-Carr) were used to seal around the porous-transport and gas-diffusion layers, respectively.

Cell Testing. For the cell testing, liquid water at 80 °C was pumped on the anode side at 100 mL/min and N_2 at 200 sccm and 100% relative humidity on the cathode side. The cell temperature was monitored on the cathode end plate and the water temperature at the anode outlet. Chronopotentiometric (CA) steps were collected for 3 min from 25 to 5000 mA total current at various intervals after conditioning the cell at 80 °C for 1 h. Average potentials of the last 30 s were used to generate polarization curves. A multichannel potentiostat (VSP300) from BioLogic equipped with electrochemical impedance spectroscopy (EIS) and a 10 A booster was used for all electrochemical cell tests. EIS data were collected from 10 mHz to 200 kHz.

RESULTS AND DISCUSSIONS

Photoreductions of chlorometallic salts were used to prepare Au-TiO_2-PC and Pt-TiO_2-PC CCSs (Figure S2). Analogous materials were also prepared using the WI method followed by thermochemical reduction (M-TiO_2-WI) using the same precursor chemicals.[41] Ir was deposited on all the M-TiO_2 materials using the WI method to generate Ir-(Au/Pt)-TiO_2-(PC/WI). The target deposition of each PGM metal on TiO_2 is 25 wt % except for the control Ir-TiO_2-WI, where we instead prepared 50 wt % Ir without the intermediate conductive layer (Table S1). The relative ratios of each element post-synthesis were determined using XRF (Figures S3 and S4). Irrespective of the precursor ratio or the irradiation duration, the Pt loading did not exceed 18 wt %, indicating that the photoreduction synthesis method utilized here is self-terminating. To investigate the effects of thermal annealing on physical properties as well as electrocatalysis, the materials were annealed at 400 °C for 2 h. The thermally treated samples are designated as "ann" hereafter (Table S1).

To probe the uniformity and morphology of the prepared catalysts, SEM, TEM, and the corresponding EDS elemental maps were collected. The SEM (Figure 2a), corresponding EDS maps (Figure 2b,c), and EDS spectrum (Figure S5) show that Pt is uniformly deposited on the TiO_2 surface when the conductive Pt layer is deposited using the PC method. As apparent from the TEM image in Figure 2g,h, Pt nanoparticles, roughly 2–3 nm in size (Figure 2i), deposit evenly on the TiO_2 surface when Pt is deposited on TiO_2 using the PC method. Furthermore, the Pt nanoparticle distribution is maintained after Ir deposition and thermal annealing (Figure 2j–m and Figure S6). Conversely, a non-uniform Au distribution in Au-TiO_2-PC is observed (Figure S7), with some areas of homogeneous coverage (Figure 2d–f). The EDS spectra for Au-TiO_2-PC in Figures S7 and S8 indicate lower loadings of Au when compared to the Pt EDS spectrum in Figure S5 even though the starting precursor ratio for both Au and Pt was 25 wt %.

Half-Cell Characterization. Using RDE, we probed the electrochemical activity of the CCS electrocatalysts with and without thermal treatment compared to the commercial baseline Umicore (IrO_2-TiO_2). The *iR* corrected OER activity in 0.1 M $HClO_4$ (Figure 3), gauged by onset potentials, was highest for Ir-Pt-TiO_2-PC > Ir-Au-TiO_2-PC > Umicore > Ir-TiO_2-WI, while the geometric current density at 1.8 V was highest for Ir-Au-TiO_2-PC > Ir-Pt-TiO_2-PC ~ Umicore > Ir-

https://dx.doi.org/10.1021/acscatal.0c03098
ACS Catal. XXXX, XXX, XXX–XXX

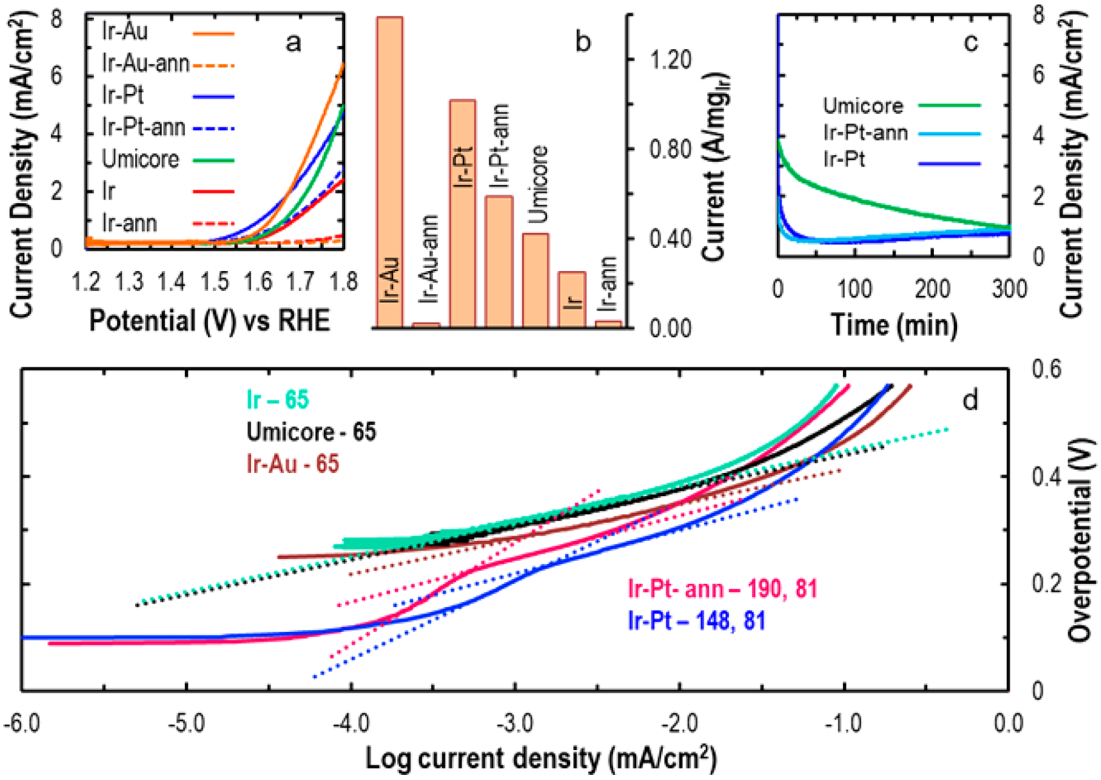

Figure 3. OER activities (*iR* corrected) of Ir catalysts supported on TiO_2. (a) Activities normalized to a geometric surface area of the working electrode. (b) OER activities at 1.8 V normalized to mg of Ir. (c) CA plots at 1.8 V. (d) Tafel plots (dotted lines) with calculated Tafel slopes (mV/dec). The electrolyte is 0.1 M $HClO_4$, the working electrode disc and counter electrode wire are gold, and the reference electrode is a dihydrogen electrode. The working electrode is rotated at 2500 rpm, and the scan rate is 20 mV/s. Total catalyst loadings on the working electrodes are 3.49 $\mu g_{Ir}/cm^2$.

TiO_2-WI. Overall, annealing was shown to have a deleterious effect on Ir-Au-TiO_2-PC and Ir-TiO_2-WI; however, Ir-Pt-TiO_2-PC-ann retained a substantial amount of its activity even slightly exceeding the commercial Umicore IrO_2-TiO_2 catalyst. Retention of excellent activity after oxidation is critical for OER catalysts intended for PEMWE because they are employed in highly oxidizing electrochemical environments. CCSs without Ir deposition do not show significant OER activities as expected (Figure S9).

While geometric OER activity of Ir-Pt-TiO_2-PC and commercial Umicore catalyst are similar at 1.8 V (Figure 3a), the benefit of employing a Pt conductive layer is demonstrated when the activities are normalized to an Ir mass loading (Figure 3b). At 1.8 V applied potential, Ir-Pt-TiO_2-PC generates 1.02 A/mg_{Ir} compared to 0.42 A/mg_{Ir} for the Umicore catalyst. This represents a 141% improvement in mass-normalized OER activity with a 42% lower PGM content (75 wt % Ir in Umicore catalyst vs 25 wt % Ir and 18 wt % Pt in Ir-Pt-TiO_2-PC). Even after thermal oxidation, the Ir-Pt-TiO_2-PC-ann catalyst generates 0.59 A/mg_{Ir} activity, that is, a 39% improvement in Ir mass-normalized OER activity. The utility of a uniform and thermally stable conductive layer is also highlighted when Ir-Pt-TiO_2-PC is compared to Ir-Au-TiO_2-PC and Ir-TiO_2 catalysts; the OER activities of those two systems drop drastically upon thermal annealing. The mass normalized activities in Figure 3b are comparable to recently reported Ir catalysts supported on TiO_2 supports (Table S2). The mass normalized activities are still a magnitude lower than the state-of-the-art unsupported[38] and antimony-doped tin oxide supported Ir catalysts.[9] However, activities of even the commercial catalysts can vary widely depending on the ink preparation methods and electrochemical conditions. Each catalyst needs to be optimized for an ionomer to catalyst ratio, sonication/stirring/shearing, and other catalyst ink preparation parameters.[38]

When the commercial catalysts and as-synthesized Pt-CCS supported materials are subjected to chronoamperometry (CA) at 1.8 V to assess initial performance, it is observed that the commercial Umicore catalyst initially generates higher geometric OER activities, but the activities converge within 5 h. Critically, the synthesized Ir-Pt-TiO_2-PC catalysts generate a similar activity after 5 h of CA to the commercial catalyst while containing 33% less PGM loading. When the as-prepared and annealed Ir-Pt-TiO_2-PC catalysts are compared (Figure 3c), the activity of as-prepared catalyst is significantly higher initially but drops precipitously to reflect that of the annealed catalyst within 30 min. The Ir-Au-TiO_2-PC catalyst, initially, also shows the highest activity at 1.8 V applied potential, but becomes inactive within minutes. Longer-term stability studies including online catalyst dissolution measurements and operando characterization of electrocatalysts are deemed beyond the scope of the current investigations.

From the Tafel slopes in Figure 3d, it is apparent that the commercial catalyst (Umicore) and as-synthesized Ir-TiO_2-WI and Ir-Au-TiO_2-PC exhibit faster OER kinetics (65 mV/dec) in comparison to Pt-containing CCS supported catalysts (81−190 mV/dec). Annealed Ir-TiO_2 and Ir-Au-TiO_2 are not included in the Tafel analysis since the activity is negligible in the relevant potential window (Figure 3a). The Tafel slopes of Pt-containing CCS supported catalysts intriguingly show two

https://dx.doi.org/10.1021/acscatal.0c03098
ACS Catal. XXXX, XXX, XXX−XXX

distinct regions. At low overpotentials (<250 mV), both as-synthesized and annealed Ir-Pt-TiO_2 catalysts show high Tafel slopes (>148 mV/dec), indicating slow kinetics but low onset potentials. At higher overpotentials (>250 mV), faster kinetics (81 mv/dec) predominate OER activity. Previous investigations on Ir and Ru via experimental and theoretical analysis have ascribed the "kink in Tafel slopes" to either different active sites or catalyst surface reorganization at different applied potentials.[42,43] These results may also indicate that the presence of the interfacial layer modulates the catalyst active site. Generally, lower Tafel slopes indicate faster kinetics and better electrochemical performance. Our observations here indicate that other effects may be affecting overall performance more dominantly than those encompassed in Tafel slopes. Further optimizations to enhance the OER kinetics coupled with the low onset potentials hold significant promise to boost overall activity of low Ir-loading CLs using supported catalysts.

Structure−Activity Relationships. In order to rationalize the trends in electrochemical activity and to understand the structure−activity relationships, we thoroughly characterized the catalysts for electronic conductivity, crystallinity, and surface composition. Conductivities of the prepared catalysts (Figure 4) show that the presence of Pt conductive layer is

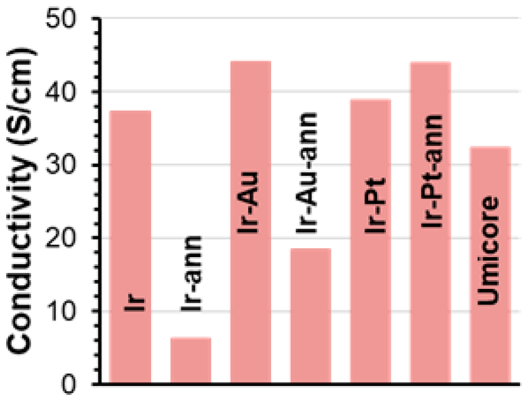

Figure 4. Electronic conductivities of various catalysts supported on TiO_2. Umicore is the commercial IrO_2-TiO_2 catalyst, and "ann" represents thermally annealed materials.

responsible for maintaining a relatively high conductivity during thermal annealing. The conductivities are similar to previous reports on various supported IrO_x catalysts prepared using the Adams fusion method (Table S4).[26,44,45] As synthesized, the Ir-TiO_2-WI, Ir-Pt-TiO_2-PC, and Ir-Au-TiO_2-PC have similar conductivities (37−44 S/cm). However, upon annealing, the conductivities of Ir-TiO_2-WI-ann and Ir-Au-TiO_2-PC-ann decrease dramatically to 6 and 18 S/cm, respectively, but the conductivity of Ir-Pt-TiO_2-PC-ann slightly improves to 44 S/cm. The observations may indicate that Ir and Au agglomerate rapidly under thermal annealing conditions (Figure S7), and they are weakly adsorbed on the TiO_2 surface. This leads to the dramatic OER activity reduction observed in Figure 3a,b. Pt however is strongly bound to the TiO_2 surface, retains conformal homogeneous distribution (Figure 2), and maintains a relatively high OER activity post-annealing.

XRD was used to investigate the crystallinity of the CCSs and catalysts. For the synthesized Pt-TiO_2-PC CCSs (Figure 5a), only TiO_2 peaks are visible in the XRD, suggesting that the PC deposition method leads to the synthesis of either an amorphous Pt layer or extremely small Pt nanoparticles. This is in agreement with the observed 2−3 nm crystalline Pt nanoparticles (Figure 2). Conversely, for the Pt-TiO_2-WI, the Pt peaks such as the Pt (111) at 39.6° are apparent. When Ir is deposited to prepare Ir-Pt-TiO_2-PC, peaks corresponding to Ir and TiO_2 are observed, but the Pt peaks remain absent. These observations indicate that Pt deposited on TiO_2 via the PC method does not aggregate under thermochemical reduction conditions during Ir deposition via the WI method to prepare Ir-Pt-TiO_2-PC. Unlike the Pt-TiO_2-WI and Ir-Pt-TiO_2-WI systems where the Pt (111) peak at 39.6° is apparent, the peak is absent for both Pt-TiO_2-PC and Ir-Pt-TiO_2-PC.

Conversely to the Pt CCSs, the XRD peaks for Au are prominent irrespective of the synthesis method (Figure 5b). The Au (111) peak at 38.1° is wider and less prominent in Ir-Au-TiO_2-PC than in Ir-Au-TiO_2-WI, indicating that the Au crystallite sizes are smaller from the PC method than from the WI method. However, as determined by electron microscopy (Figure S7) and visual observations, the Au precursor is photosensitive, and some portion of it is readily reduced upon exposure to ambient light without semiconductor-assisted photoreduction. It is likely that the Au peaks in Ir-Au-TiO_2-PC are from the initial precipitation rather than PC reduction on TiO_2 surface. However, akin to Ir-Pt-TiO_2-PC, the Au peaks in Au-TiO_2-PC do not show significant aggregation or crystallite size coarsening during the Ir deposition via the WI method.

Curiously, Ir-Pt-TiO_2-PC does not show Pt or Ir oxidation during thermal treatment, as apparent from Figure 5c, with no significant peaks corresponding to iridium oxides (IrO_x) or platinum oxides (PtO_x). However, the Au and Ir are oxidized to Au_2O_3 and IrO_2 for Ir-Au-TiO_2-PC-ann. The observations indicate that the Pt interlayer may have a stabilizing effect on Ir with respect to oxidation, and the bulk of Pt itself does not oxidize. The oxidation and aggregation lead to both conductivity reduction (Figure 4) and activity loss (Figure 3) for Ir-TiO_2-WI and Ir-Au-TiO_2-PC-ann, but Ir-Pt-TiO_2-PC is thermally stable and maintains high conductivity and activity. Particle size analysis shows that crystallite sizes generally increase upon annealing (Table S3). The Pt CCS supported Ir crystallite size increases from 10 to 28 nm, while the crystallite size of the commercial supported Ir catalyst is 9 nm. Thus, some of the activity loss can be attributed to agglomeration and loss in the active surface area.

Collectively, the XRD (Figure 5), microscopy (Figure 2), and electrochemical activity trends (Figure 3) also point to a subtle difference in how Au and Pt reductions and depositions may proceed. By the eye, the Au precursor decomposes rapidly when exposed to ambient light, forming a precipitate. However, the slow evolution of color (darkening) during PC irradiation indicates that some Au precursor remains in the solution and is reduced at a much slower rate to metallic Au nanoparticles under PC irradiation (Figure S2). These Au nanoparticles agglomerate during the Ir deposition via the WI method to prepare Ir-Au-TiO_2-PC and thermal treatment to generate Ir-Au-TiO_2-PC-ann. We chose not to employ strategies such as the use of surfactants or dilute precursors to prevent Au nanoparticle formation and aggregation due to the associated complications with post-synthesis purification steps. The Pt deposition in contrast occurs by photoreduction at the TiO_2 surface, that is, semiconductor-assisted photo-driven reduction to form Pt-TiO_2-PC. The process thus leads to Pt nanoparticles evenly distributed on a TiO_2 surface, and strong adsorption to the substrate prevents Pt nanoparticle

https://dx.doi.org/10.1021/acscatal.0c03098
ACS Catal. XXXX, XXX, XXX−XXX

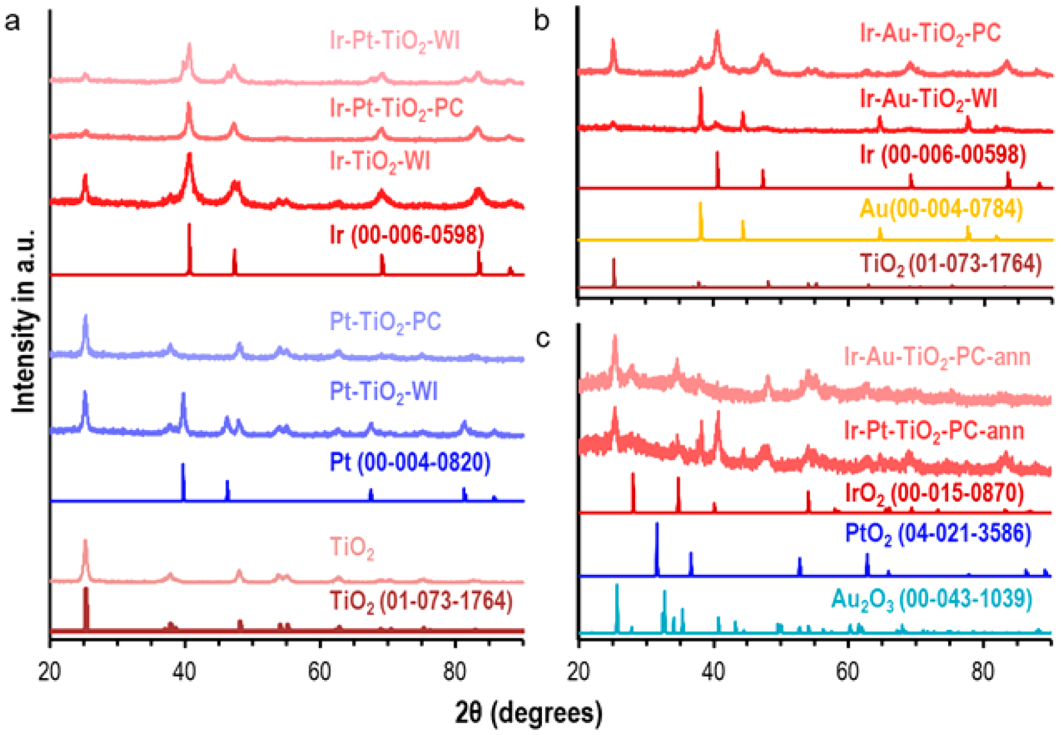

Figure 5. XRD diffraction patterns for: (a) Pt coated CCSs (blue) and Ir supported on CCSs (red). (b) Ir supported on Au coated CCSs and (c) effects of thermal annealing in air for Ir deposited on CCSs synthesized via PC reduction. Diffraction pattern of as-obtained TiO_2 nanoparticles (TiO_2) is included in (a), and all the reference patterns are accompanied by corresponding PDF numbers.

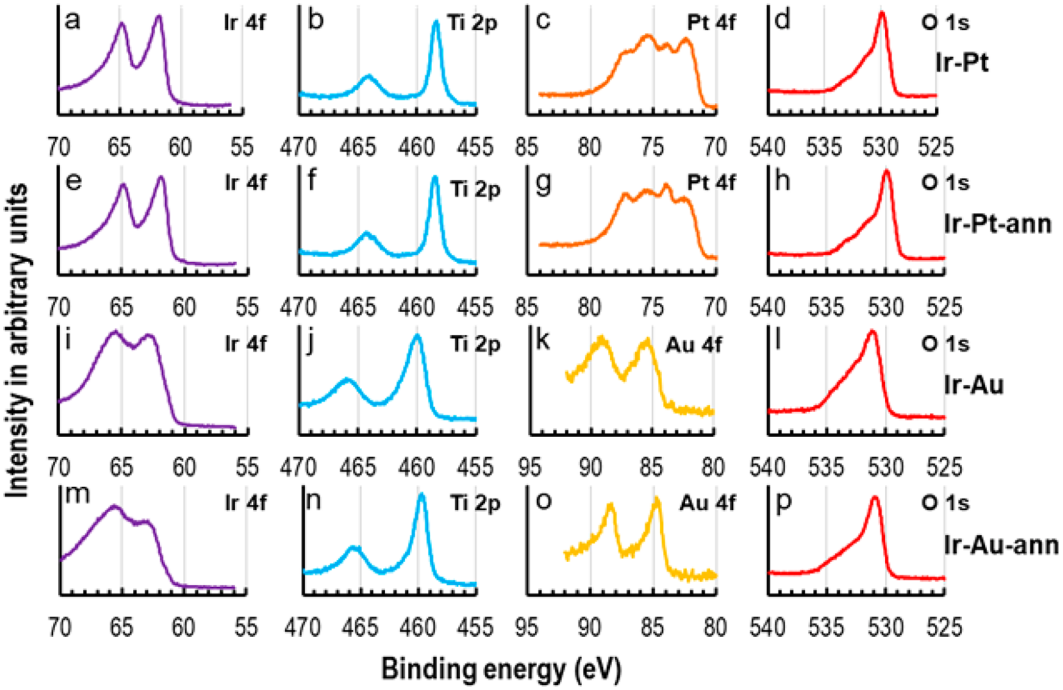

Figure 6. XPS spectra of Ir catalysts supported on CCSs synthesized using a photochemical reduction method. (a–d) Ir-Pt-TiO_2-PC, (e–h) Ir-Pt-TiO_2-PC-ann, (i–l) Ir-Au-TiO_2-PC, and (m–p) Ir-Au-TiO_2-PC-ann. The spectra are as collected without background correction.

aggregation during WI reduction to prepare Ir-Pt-TiO_2-PC and thermal treatment steps to prepare Ir-Pt-TiO_2-PC-ann.

By XPS (Figure 6), it is apparent that the majority of the near surface Ir deposited on Pt CCSs is IrO_2 with some metallic (Ir^0) characteristic, apparent from the core Ir 4f binding energies (i.e., Ir $4f_{7/2}$ at 61.9 eV and Ir $4f_{5/2}$ at 64.9 eV, respectively).[46,47] The XPS spectrum for Ir-Pt-TiO_2-PC does not change before and after annealing in air, as apparent from the Ir 4f region (Figure 6a,e). There is, however, an increased level of Ir oxidation after annealing for Ir-Au-TiO_2-PC, as apparent from the change in Ir 4f spectra in Figure 6i,m.[48] For the Ir deposited on Au CCSs (Figure 6i,m) and bare TiO_2

https://dx.doi.org/10.1021/acscatal.0c03098
ACS Catal. XXXX, XXX, XXX−XXX

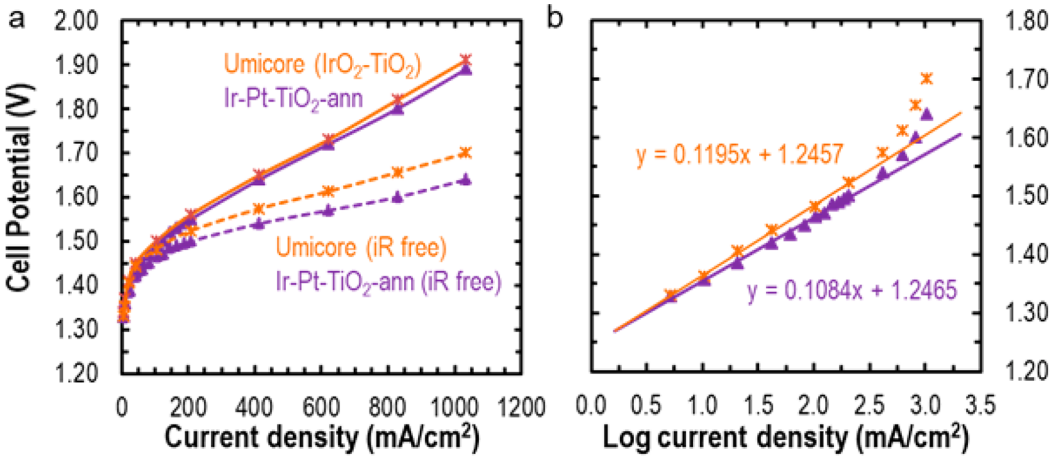

Figure 7. (a) Electrolyzer polarization curves using annealed Ir-Pt-TiO_2 and commercial Umicore catalysts at 1.0 mg/cm^2 PGM on the anode, 0.3 mg/cm^2 Pt (Pt/C) on the cathode, and liquid water feeds at 80 °C and N117 membranes. (b) Tafel plots of *iR* free polarization curves with the corresponding equations in the kinetics region.

(Figure S10), the Ir is mostly oxidized (IrO_2) with Ir $4f_{7/2}$ at 63 eV and Ir $4f_{5/2}$ at 66 eV. In agreement with the XRD (Figure 5c), XPS confirms that Ir deposited on Pt CCS is more metallic in nature relative to Ir deposited on Au CCS. Furthermore, the Ti 2p peaks are at lower binding energies for Ir-Pt-TiO_2-PC before and after annealing (Figure 6b,f), in comparison to, both, Ir-Au-TiO_2-PC (Figure 6j,n), and for Ir-TiO_2 (Figure S10). Similarly, the O 1s peaks for Ir-Pt-TiO_2-PC also appear at about 1 eV lower than that of Ir-Au-TiO_2-PC and Ir-TiO_2-WI. However, there is a significant change in the Pt 4f spectrum for Ir-Pt-TiO_2-PC. There is an increase in Pt^{2+} (74 eV) with respect to Pt^0 (72 eV) after annealing.[49] Au 4f peaks show a slight shift to lower binding energy upon annealing as the full width at half-maximum gets smaller (Figure 6k,o).

The difference in the minima between the Ir 4f peaks in Figure 6i for Ir-Au-TiO_2 compared to that of Ir-Pt-TiO_2 (Figure 6a) has previously been rationalized as the interference from the Ti 3s peak by Aguilar-Tapia et al.[50] From the comparison of the XPS spectra, it is evident that the direct interaction between Ir and TiO_2 leads to higher binding energy shifts for Ir and Ti, while an interlayer of Pt prevents Ir and Ti from influencing each other's binding energies. The observations from XPS further confirm that Au does not form a uniform layer on TiO_2 to act as an interlayer between Ir and TiO_2. Ir-Au-TiO_2-PC behaves more akin to Ir-TiO_2 than Ir-Pt-TiO_2-PC during thermal annealing. Additionally, there is evidence of a charge transfer from Ir to Pt, which leads to Pt itself oxidizing during annealing (Figure 6c,g) and consequently Ir retaining a metallic character.[46,51] In agreement with previous studies of Au-IrO_2 composites, Au on the contrary leads to increased Ir oxidation since the binding energies of Au 4f peaks shift slightly lower.[52] The stability of the Ir surfaces deposited on Pt-CCSs evidenced from XPS spectra in Figure 6 directly correlate to the retention of high OER activities in Figure 3. Furthermore, the drastic loss in the OER activities of Au-CCS and TiO_2 supported Ir upon thermal annealing highlights the utility of using a stable conformal conductive layer between the OER Ir catalysts and the non-PGM TiO_2 cores.

PEMWE Performance. As a preliminary proof-of-concept demonstration for catalyst integration into a MEA, the most promising CCS catalyst (Ir-Pt-TiO_2-PC-ann) was integrated into a PEMWE cell with 1.0 mg/cm^2 PGM loadings on the anode and 0.3 mg/cm^2 Pt (Pt/C) on the cathode and compared with the commercial TiO_2 supported Umicore catalyst at the same anode catalyst loadings. The balance of cell components, the membrane, the pretreatment conditions, and the testing conditions are described elsewhere.[39] From the polarization curves at 80 °C in Figure 7a, it is apparent that the Ir-Pt-TiO_2-PC-ann catalyst outperforms the commercial Umicore catalyst. It must also be emphasized that the CCS supported catalysts are yet to be optimized for CL integration and MEA performance, which is beyond the scope of this work. Additionally, it is also well established that each OER Ir catalyst requires a unique set of catalyst ink preparation and catalyst layer fabrication methods to perform optimally.[53] Nevertheless, the CCS supported catalysts outperform previously reported TiO_2 supported Ir catalysts assessed under similar testing conditions after optimization (Table S4).[25,54,55] However, as with half-cell activities, the MEA performances are still significantly inferior to state-of-the-art unsupported IrO_x catalysts (Table S5).[15] Ir-Pt-TiO_2-PC-ann achieves 1 A/cm^2 activity at 1.87 V, while the Umicore catalyst requires 1.89 V.

High-frequency resistances (HFRs), which account for ohmic losses of the entire cell, were used to generate *iR*-corrected polarization curves in Figure 7a.[56] The Tafel analysis in Figure 7b indicates that the OER kinetics of Ir-Pt-TiO_2-PC are superior (108 mV/dec) to the Umicore catalyst (120 mV/dec). The trend is in contrast to half-cell observations in Figure 3d, which showed lower Tafel slopes for Umicore catalysts (65 mV/dec) than for Ir-Pt-TiO_2-PC (81 mV/dec). The observation re-emphasizes that RDE performances are not always translatable to cell performance. The HFR-corrected polarization curves (Figure 7a) also allow a MEA performance comparison among various membrane thicknesses. From Table S5, it is apparent that the CCS supported catalysts generate comparable activities to other oxide supported IrO_x catalysts at 1 A/cm^2 under similar conditions and cell configuration. As with the half-cell analysis in Figure 3 however, further optimizations in catalyst structure, ink composition, and catalyst integration methods are necessary to match the performances of the state-of-the-art catalysts and catalyst layers.

https://dx.doi.org/10.1021/acscatal.0c03098
ACS Catal. XXXX, XXX, XXX−XXX

CL thickness and porosity also influence the performance by improving transport. Cross-sectional SEM of the MEA illustrates that the CL thickness increased and the porosity was manipulated by employing CCS supports (Figure S11). The anode CL thickness is comparable to previous reports using 2−3 mg/cm^2 PGM catalyst loadings.[22,40,54,57−59] Further investigations are underway to understand the contributions of the kinetics, mass transport, catalyst layer fabrication methods, and catalyst ink compositions in electrolyzer performance using CCS integrated CLs.

CONCLUSIONS

We have demonstrated a facile photoreduction method to generate a conformal layer of platinum nanoparticles on TiO_2, forming conductive layer coated supports (CCSs). The conductive intermediate layer prevents bulk iridium oxidation in the Ir-Pt-TiO_2 catalyst during annealing and improves the composite electrocatalyst conductivity at a significantly lower precious group metal (PGM) loading (39 wt %) in comparison to a TiO_2 supported commercial catalyst with 75 wt % PGM loading. Photoreduction generated a conformal platinum layer that is strongly bound to the semiconductor surface and is stable in thermochemical and electrochemical environments. The presented X-ray photoelectron spectroscopy, X-ray diffraction, and electron microscopy images show significant opportunities to further engineer highly active and stable surfaces, interfaces, and active sites utilizing the conductive interlayer in comparison to bare TiO_2 supports. The half-cell oxygen evolution reaction (OER) activities show that the Pt-CCS supported iridium generates a 141% higher OER mass activity than the commercial TiO_2 supported catalyst from Umicore. Furthermore, the single-cell performance of the CCS supported catalyst reveals a superior performance to other supported catalysts reported thus far, even prior to any integration and fabrication optimizations. Our investigations also reaffirm that translating the half-cell catalyst performance to device level performance requires considerable optimization during the catalyst layer fabrication and device integration. We expect future investigations utilizing CCSs to improve the electrolyzer performance significantly from CCS supported materials and device optimization via synthetic modifications as well as targeted catalyst ink preparation for each catalyst and cell fabrication methodologies.

ASSOCIATED CONTENT

Supporting Information

The Supporting Information is available free of charge at https://pubs.acs.org/doi/10.1021/acscatal.0c03098.

Synthesis routes, table of catalysts used in the investigation, additional SEM images and EDS maps, EDS spectra, XPS plots, XRF data, OER data corresponding to CCS only materials, and table of MEA performance of TiO_2 supported Ir catalysts from recent investigations (PDF)

Video S1: Generation of conductive layer coated catalyst substrates via photoreduction (AVI)

AUTHOR INFORMATION

Corresponding Author

Nemanja Danilovic − *Energy Storage and Distributed Resources Division, Lawrence Berkeley National Laboratory, Berkeley, California 94720, United States*; Email: ndanilovic@lbl.gov

Authors

Yagya N. Regmi − *Energy Storage and Distributed Resources Division, Lawrence Berkeley National Laboratory, Berkeley, California 94720, United States; Department of Chemistry, Manchester Metropolitan University, Manchester M1 5GD, United Kingdom*; orcid.org/0000-0001-6588-7683

Eden Tzanetopoulos − *Energy Storage and Distributed Resources Division, Lawrence Berkeley National Laboratory, Berkeley, California 94720, United States; College of Chemistry, University of California Berkeley, Berkeley, California 94720, United States*

Guosong Zeng − *Chemical Sciences Division and Joint Center for Artificial Photosynthesis, Lawrence Berkeley National Laboratory, Berkeley, California 94720, United States*

Xiong Peng − *Energy Storage and Distributed Resources Division, Lawrence Berkeley National Laboratory, Berkeley, California 94720, United States*

Douglas I. Kushner − *Energy Storage and Distributed Resources Division, Lawrence Berkeley National Laboratory, Berkeley, California 94720, United States*; orcid.org/0000-0002-3020-7737

Tobias A. Kistler − *Chemical Sciences Division and Joint Center for Artificial Photosynthesis, Lawrence Berkeley National Laboratory, Berkeley, California 94720, United States; Walter Schottky Institute and Physics Department, Technische Universität München, 85748 Garching, Germany*; orcid.org/0000-0001-6458-8024

Laurie A. King − *Department of Chemistry, Manchester Metropolitan University, Manchester M1 5GD, United Kingdom*; orcid.org/0000-0002-0772-2378

Complete contact information is available at: https://pubs.acs.org/10.1021/acscatal.0c03098

Author Contributions

N.D. and Y.R. conceived the project and secured funding. Y.R., E.T., L.K., and N.D. conceived synthesis routes and/or synthesized the materials. Y.R. and E.T. conducted XRD and SEM/EDS. Y.R., E.T., and X.P. conducted STEM/EDS. Y.R., G.Z., and L.K. collected and analyzed XPS. Y.R., E.T., and N.D. conducted and analyzed electrochemical measurements. T.K. operated the solar simulator lamp and associated camera. D.K. designed the conductivity setup. Y.R. and E.T. composed the manuscript, and all the authors edited the written work under the leadership of N.D.

Notes

The authors declare no competing financial interest.

ACKNOWLEDGMENTS

The authors acknowledge the Department of Energy, Office of Energy Efficiency and Renewable Energy, Fuel Cell Technologies Office (DOE-EERE-FCTO) and program manager David Peterson for funding under contract number DE-AC02-05CH11231. Transmission electron microscopy work at the Molecular Foundry was supported by the Office of Science, Office of Basic Energy Sciences, of the U.S. Department of Energy under contract no. DE-AC02-05CH11231. We also thank Adam Z. Weber, group leader for the Energy Conversion group at Berkeley National Laboratories, for advice and guidance throughout. We also thank the National Center for Electron Microscopy (NCEM) scientists Chengyu Song, Karen Bustillo, and Rohan Dhall for electron microscopy guidance and training and the Joint Center for Artificial

https://dx.doi.org/10.1021/acscatal.0c03098
ACS Catal. XXXX, XXX, XXX−XXX

Photosynthesis scientists Francesca Toma, Jason Cooper, Peter Agbo, and David Larson for access to XRD, SEM, XPS, solar simulator, centrifuge, and tube furnace as affiliates through the HydroGEN Consortium. We also thank Proton OnSite/NEL for Ti PTLs.

REFERENCES

(1) Tilley, S. D. Recent Advances and Emerging Trends in Photo-Electrochemical Solar Energy Conversion. *Adv. Energy Mater.* **2019**, *9* (2), 1802877.

(2) Ayers, K.; Danilovic, N.; Ouimet, R.; Carmo, M.; Pivovar, B.; Bornstein, M. Perspectives on Low-Temperature Electrolysis and Potential for Renewable Hydrogen at Scale. *Annu. Rev. Chem. Biomol. Eng.* **2019**, *10*, 219−239.

(3) Quarton, C. J.; Samsatli, S. The value of hydrogen and carbon capture, storage and utilisation in decarbonising energy: Insights from integrated value chain optimization. *Appl. Energy* **2020**, *257*, 113936.

(4) Staffell, I.; Scamman, D.; Velazquez Abad, A.; Balcombe, P.; Dodds, P. E.; Ekins, P.; Shah, N.; Ward, K. R. The role of hydrogen and fuel cells in the global energy system. *Energy Environ. Sci.* **2019**, *12* (2), 463−491.

(5) Pivovar, B.; Rustagi, N.; Satyapal, S. Hydrogen at Scale (H2@ Scale): Key to a Clean, Economic, and Sustainable Energy System. *Electrochem. Soc. Interface* **2018**, *27* (1), 47−52.

(6) Peterson, D.; Vickers, J.; DeSantis, D. *Hydrogen Production Cost From PEM Electrolysis - 2019*; Department of Energy: Washington, DC, 2020; p 15.

(7) James, B. D.; DeSantis, D. A.; Saur, G. *Final Report: Hydrogen Production Pathways Cost Analysis (2013 − 2016)*; U.S. Department of Energy Office of Scientific and Technical Information: Oak Ridge, TN, 2016. DOI: 10.2172/1346418.

(8) Schmidt, O.; Melchior, S.; Hawkes, A.; Staffell, I. Projecting the Future Levelized Cost of Electricity Storage Technologies. *Joule* **2019**, *3* (1), 81−100.

(9) Oh, H. S.; Nong, H. N.; Reier, T.; Bergmann, A.; Gliech, M.; Ferreira de Araujo, J.; Willinger, E.; Schlogl, R.; Teschner, D.; Strasser, P. Electrochemical Catalyst-Support Effects and Their Stabilizing Role for IrOx Nanoparticle Catalysts during the Oxygen Evolution Reaction. *J. Am. Chem. Soc.* **2016**, *138* (38), 12552−63.

(10) Shi, Q.; Zhu, C.; Du, D.; Lin, Y. Robust noble metal-based electrocatalysts for oxygen evolution reaction. *Chem. Soc. Rev.* **2019**, *48* (12), 3181−3192.

(11) Pham, C. V.; Bühler, M.; Knöppel, J.; Bierling, M.; Seeberger, D.; Escalera-López, D.; Mayrhofer, K. J. J.; Cherevko, S.; Thiele, S. IrO2 coated TiO2 core-shell microparticles advance performance of low loading proton exchange membrane water electrolyzers. *Appl. Catal., B* **2020**, *269*, 118762.

(12) Nong, H. N.; Reier, T.; Oh, H.-S.; Gliech, M.; Paciok, P.; Vu, T. H. T.; Teschner, D.; Heggen, M.; Petkov, V.; Schlögl, R.; Jones, T.; Strasser, P. A unique oxygen ligand environment facilitates water oxidation in hole-doped IrNiOx core−shell electrocatalysts. *Nature Catalysis* **2018**, *1* (11), 841−851.

(13) Lei, Z. W.; Wang, T. Y.; Zhao, B. T.; Cai, W. B.; Liu, Y.; Jiao, S. H.; Li, Q.; Cao, R. G.; Liu, M. L. Recent Progress in Electrocatalysts for Acidic Water Oxidation. *Adv. Energy Mater.* **2020**, *10* (23), 2000478.

(14) King, L. A.; Hubert, M. A.; Capuano, C.; Manco, J.; Danilovic, N.; Valle, E.; Hellstern, T. R.; Ayers, K.; Jaramillo, T. F. A non-precious metal hydrogen catalyst in a commercial polymer electrolyte membrane electrolyser. *Nat. Nanotechnol.* **2019**, *14* (11), 1071−1074.

(15) Alia, S. M.; Stariha, S.; Borup, R. L. Electrolyzer Durability at Low Catalyst Loading and with Dynamic Operation. *J. Electrochem. Soc.* **2019**, *166* (15), F1164−F1172.

(16) Jorge, A. B.; Jervis, R.; Periasamy, A. P.; Qiao, M.; Feng, J.; Tran, L. N.; Titirici, M. M. 3D Carbon Materials for Efficient Oxygen and Hydrogen Electrocatalysis. *Adv. Energy Mater.* **2020**, *10* (11), 1902494.

(17) Frydendal, R.; Paoli, E. A.; Chorkendorff, I.; Rossmeisl, J.; Stephens, I. E. L. Toward an Active and Stable Catalyst for Oxygen Evolution in Acidic Media: Ti-Stabilized MnO2. *Adv. Energy Mater.* **2015**, *5* (22), 1500991.

(18) Reier, T.; Nong, H. N.; Teschner, D.; Schlögl, R.; Strasser, P. Electrocatalytic Oxygen Evolution Reaction in Acidic Environments - Reaction Mechanisms and Catalysts. *Adv. Energy Mater.* **2017**, *7* (1), 1601275.

(19) Bernt, M.; Hartig-Weiß, A.; Tovini, M. F.; El-Sayed, H. A.; Schramm, C.; Schröter, J.; Gebauer, C.; Gasteiger, H. A. Current Challenges in Catalyst Development for PEM Water Electrolyzers. *Chem. Ing. Tech.* **2020**, *92* (1−2), 31−39.

(20) Horton, F., XLIII The electrical conductivity of metallic oxides. *London, Edinburgh, and Dublin Philosophical Magazine and Journal of Science* **1906**, *11* (64), 505−531.

(21) Han, B.; Risch, M.; Belden, S.; Lee, S.; Bayer, D.; Mutoro, E.; Shao-Horn, Y. Screening Oxide Support Materials for OER Catalysts in Acid. *J. Electrochem. Soc.* **2018**, *165* (10), F813−F820.

(22) Kang, X.; Liu, S.; Dai, Z.; He, Y.; Song, X.; Tan, Z. Titanium Dioxide: From Engineering to Applications. *Catalysts* **2019**, *9* (2), 191.

(23) Nunes, B. N.; Lopes, O. F.; Patrocinio, A. O. T.; Bahnemann, D. W. Recent Advances in Niobium-Based Materials for Photo-catalytic Solar Fuel Production. *Catalysts* **2020**, *10* (1), 126.

(24) Hegge, F.; Moroni, R.; Trinke, P.; Bensmann, B.; Hanke-Rauschenbach, R.; Thiele, S.; Vierrath, S. Three-dimensional microstructure analysis of a polymer electrolyte membrane water electrolyzer anode. *J. Power Sources* **2018**, *393*, 62−66.

(25) Wang, C.; Lan, F.; He, Z.; Xie, X.; Zhao, Y.; Hou, H.; Guo, L.; Murugadoss, V.; Liu, H.; Shao, Q.; Gao, Q.; Ding, T.; Wei, R.; Guo, Z. Iridium-Based Catalysts for Solid Polymer Electrolyte Electro-catalytic Water Splitting. *ChemSusChem* **2019**, *12* (8), 1576−1590.

(26) Oakton, E.; Lebedev, D.; Fedorov, A.; Krumeich, F.; Tillier, J.; Sereda, O.; Schmidt, T. J.; Copéret, C. A simple one-pot Adams method route to conductive high surface area IrO2−TiO2 materials. *New J. Chem.* **2016**, *40* (2), 1834−1838.

(27) Bernt, M.; Gasteiger, H. A. Influence of Ionomer Content in IrO2/TiO2Electrodes on PEM Water Electrolyzer Performance. *J. Electrochem. Soc.* **2016**, *163* (11), F3179−F3189.

(28) Alia, S. M.; Rasimick, B.; Ngo, C.; Neyerlin, K. C.; Kocha, S. S.; Pylypenko, S.; Xu, H.; Pivovar, B. S. Activity and Durability of Iridium Nanoparticles in the Oxygen Evolution Reaction. *J. Electrochem. Soc.* **2016**, *163* (11), F3105−F3112.

(29) Vesborg, P. C. K.; Jaramillo, T. F. Addressing the terawatt challenge: scalability in the supply of chemical elements for renewable energy. *RSC Adv.* **2012**, *2* (21), 7933.

(30) Mayyas, A. T.; Ruth, M. F.; Pivovar, B. S.; Bender, G.; Wipke, K. B. *Manufacturing Cost Analysis for Proton Exchange Membrane Water Electrolyzers*; U.S. Department of Energy Office of Scientific and Technical Information: Oak Ridge, TN, 2019. DOI: 10.2172/1557965.

(31) Yoon, W.; Huang, X.; Fazzino, P.; Reifsnider, K. L.; Akkaoui, M. A. Evaluation of coated metallic bipolar plates for polymer electrolyte membrane fuel cells. *J. Power Sources* **2008**, *179* (1), 265−273.

(32) Kumar, A.; Ricketts, M.; Hirano, S. Ex situ evaluation of nanometer range gold coating on stainless steel substrate for automotive polymer electrolyte membrane fuel cell bipolar plate. *J. Power Sources* **2010**, *195* (5), 1401−1407.

(33) Lettenmeier, P.; Kolb, S.; Sata, N.; Fallisch, A.; Zielke, L.; Thiele, S.; Gago, A. S.; Friedrich, K. A. Comprehensive investigation of novel pore-graded gas diffusion layers for high-performance and cost-effective proton exchange membrane electrolyzers. *Energy Environ. Sci.* **2017**, *10* (12), 2521−2533.

(34) Qiao, Z.; Hwang, S.; Li, X.; Wang, C.; Samarakoon, W.; Karakalos, S.; Li, D.; Chen, M.; He, Y.; Wang, M.; Liu, Z.; Wang, G.; Zhou, H.; Feng, Z.; Su, D.; Spendelow, J. S.; Wu, G. 3D porous graphitic nanocarbon for enhancing the performance and durability of

https://dx.doi.org/10.1021/acscatal.0c03098
ACS Catal. XXXX, XXX, XXX−XXX

Pt catalysts: a balance between graphitization and hierarchical porosity. *Energy Environ. Sci.* **2019**, *12* (9), 2830−2841.
(35) Steimle, B. C.; Fenton, J. L.; Schaak, R. E. Rational construction of a scalable heterostructured nanorod megalibrary. *Science* **2020**, *367* (6476), 418−424.
(36) Petrovick, J. G.; Kushner, D. I.; Tesfaye, M.; Danilovic, N.; Radke, C. J.; Weber, A. Z. Mass-Transport Resistances of Acid and Alkaline Ionomer Layers: A Microelectrode Study Part 1 - Microelectrode Development. *ECS Trans.* **2019**, *92* (8), 77−85.
(37) Kistler, T. A.; Danilovic, N.; Agbo, P. Editors' Choice—A Monolithic Photoelectrochemical Device Evolving Hydrogen in Pure Water. *J. Electrochem. Soc.* **2019**, *166* (13), H656−H661.
(38) Alia, S. M.; Anderson, G. C. Iridium Oxygen Evolution Activity and Durability Baselines in Rotating Disk Electrode Half-Cells. *J. Electrochem. Soc.* **2019**, *166* (4), F282−F294.
(39) Regmi, Y. N.; Peng, X.; Fornaciari, J. C.; Wei, M.; Myers, D. J.; Weber, A. Z.; Danilovic, N. A low temperature unitized regenerative fuel cell realizing 60% round trip efficiency and 10 000 cycles of durability for energy storage applications. *Energy Environ. Sci.* **2020**, *13* (7), 2096−2105.
(40) Stahler, M.; Stahler, A.; Scheepers, F.; Carmo, M.; Stolten, D. A completely slot die coated membrane electrode assembly. *Int. J. Hydrogen Energy* **2019**, *44* (14), 7053−7058.
(41) Regmi, Y. N.; Waetzig, G. R.; Duffee, K. D.; Schmuecker, S. M.; Thode, J. M.; Leonard, B. M. Carbides of group IVA, VA and VIA transition metals as alternative HER and ORR catalysts and support materials. *J. Mater. Chem. A* **2015**, *3* (18), 10085−10091.
(42) Dickens, C. F.; Kirk, C.; Nørskov, J. K. Insights into the Electrochemical Oxygen Evolution Reaction with ab Initio Calculations and Microkinetic Modeling: Beyond the Limiting Potential Volcano. *J. Phys. Chem. C* **2019**, *123* (31), 18960−18977.
(43) Stoerzinger, K. A.; Qiao, L.; Biegalski, M. D.; Shao-Horn, Y. Orientation-Dependent Oxygen Evolution Activities of Rutile IrO2 and RuO2. *J. Phys. Chem. Lett.* **2014**, *5* (10), 1636−41.
(44) Mazúr, P.; Polonský, J.; Paidar, M.; Bouzek, K. Non-conductive TiO2 as the anode catalyst support for PEM water electrolysis. *Int. J. Hydrogen Energy* **2012**, *37* (17), 12081−12088.
(45) Hao, C.; Lv, H.; Mi, C.; Song, Y.; Ma, J. Investigation of Mesoporous Niobium-Doped TiO2 as an Oxygen Evolution Catalyst Support in an SPE Water Electrolyzer. *ACS Sustainable Chem. Eng.* **2016**, *4* (3), 746−756.
(46) Freakley, S. J.; Ruiz-Esquius, J.; Morgan, D. J. The X-ray photoelectron spectra of Ir, IrO2 and IrCl3 revisited. *Surf. Interface Anal.* **2017**, *49* (8), 794−799.
(47) Pfeifer, V.; Jones, T. E.; Velasco Vélez, J. J.; Massué, C.; Arrigo, R.; Teschner, D.; Girgsdies, F.; Scherzer, M.; Greiner, M. T.; Allan, J.; Hashagen, M.; Weinberg, G.; Piccinin, S.; Hävecker, M.; Knop-Gericke, A.; Schlögl, R. The electronic structure of iridium and its oxides. *Surf. Interface Anal.* **2016**, *48* (5), 261−273.
(48) Siracusano, S.; Van Dijk, N.; Payne-Johnson, E.; Baglio, V.; Aricò, A. S. Nanosized IrOx and IrRuOx electrocatalysts for the O2 evolution reaction in PEM water electrolysers. *Appl. Catal., B* **2015**, *164*, 488−495.
(49) Haselmann, G. M.; Eder, D. Early-Stage Deactivation of Platinum-Loaded TiO2 Using In Situ Photodeposition during Photocatalytic Hydrogen Evolution. *ACS Catal.* **2017**, *7* (7), 4668−4675.
(50) Aguilar-Tapia, A.; Zanella, R.; Calers, C.; Louis, C.; Delannoy, L. Synergistic effects of Ir-Au/TiO(2) catalysts in the total oxidation of propene: influence of the activation conditions. *Phys. Chem. Chem. Phys.* **2015**, *17* (42), 28022−32.
(51) Haverkamp, R. G.; Marshall, A. T.; Cowie, B. C. C. Energy resolved XPS depth profile of (IrO2, RuO2, Sb2O5, SnO2) electrocatalyst powder to reveal core-shell nanoparticle structure. *Surf. Interface Anal.* **2011**, *43* (5), 847−855.
(52) de Freitas, I. C.; Parreira, L. S.; Barbosa, E. C. M.; Novaes, B. A.; Mou, T.; Alves, T. V.; Quiroz, J.; Wang, Y. C.; Slater, T. J.; Thomas, A.; Wang, B.; Haigh, S. J.; Camargo, P. H. C. Design-controlled synthesis of IrO2 sub-monolayers on Au nanoflowers: marrying plasmonic and electrocatalytic properties. *Nanoscale* **2020**, *12* (23), 12281−12291.
(53) Bender, G.; Carmo, M.; Smolinka, T.; Gago, A.; Danilovic, N.; Mueller, M.; Ganci, F.; Fallisch, A.; Lettenmeier, P.; Friedrich, K. A.; Ayers, K.; Pivovar, B.; Mergel, J.; Stolten, D. Initial approaches in benchmarking and round robin testing for proton exchange membrane water electrolyzers. *Int. J. Hydrogen Energy* **2019**, *44* (18), 9174−9187.
(54) Lv, H.; Zhang, G.; Hao, C.; Mi, C.; Zhou, W.; Yang, D.; Li, B.; Zhang, C. Activity of IrO2 supported on tantalum-doped TiO2 electrocatalyst for solid polymer electrolyte water electrolyzer. *RSC Adv.* **2017**, *7* (64), 40427−40436.
(55) Lv, H.; Wang, S.; Hao, C.; Zhou, W.; Li, J.; Xue, M.; Zhang, C. Oxygen-Deficient Ti0.9Nb0.1O2-x as an Efficient Anodic Catalyst Support for PEM Water Electrolyzer. *ChemCatChem* **2019**, *11* (10), 2511−2519.
(56) Kang, Z.; Mo, J.; Yang, G.; Retterer, S. T.; Cullen, D. A.; Toops, T. J.; Green, J. B., Jr; Mench, M. M.; Zhang, F.-Y. Investigation of thin/well-tunable liquid/gas diffusion layers exhibiting superior multifunctional performance in low-temperature electrolytic water splitting. *Energy Environ. Sci.* **2017**, *10* (1), 166−175.
(57) Babic, U.; Tarik, M.; Schmidt, T. J.; Gubler, L. Understanding the effects of material properties and operating conditions on component aging in polymer electrolyte water electrolyzers. *J. Power Sources* **2020**, *451*, 227778.
(58) Schuler, T.; Ciccone, J. M.; Krentscher, B.; Marone, F.; Peter, C.; Schmidt, T. J.; Büchi, F. N. Hierarchically Structured Porous Transport Layers for Polymer Electrolyte Water Electrolysis. *Adv. Energy Mater.* **2020**, *10* (2), 1903216.
(59) Hao, C.; Lv, H.; Zhao, Q.; Li, B.; Zhang, C.; Mi, C.; Song, Y.; Ma, J. Investigation of V-doped TiO2 as an anodic catalyst support for SPE water electrolysis. *Int. J. Hydrogen Energy* **2017**, *42* (15), 9384−9395.

https://dx.doi.org/10.1021/acscatal.0c03098
ACS Catal. XXXX, XXX, XXX−XXX